

Impact of combinations of time-delay interferometry channels on stochastic gravitational wave background detection

Zheng-Cheng Liang,¹ Zhi-Yuan Li,¹ Jun Cheng,¹ En-Kun Li,¹ Jian-dong Zhang,¹ and Yi-Ming Hu^{1,*}

¹MOE Key Laboratory of TianQin Mission, TianQin Research Center for Gravitational Physics & School of Physics and Astronomy, Frontiers Science Center for TianQin, CNSA Research Center for Gravitational Waves, Sun Yat-sen University (Zhuhai Campus), Zhuhai 519082, China

(Dated: May 23, 2023)

The method of time delay interferometry (TDI) is proposed to cancel the laser noise in space-borne gravitational-wave detectors. Among all different TDI combinations, the most commonly used ones are the orthogonal channels A, E and T, where A and E are signal-sensitive and T is signal-insensitive. Meanwhile, for the detection of stochastic gravitational-wave background, one needs to introduce the overlap reduction function to characterize the correlation between channels. For the calculation of overlap reduction function, it is often convenient to work in the low-frequency approximation, and assuming the equal-arm Michelson channels. However, if one wishes to work on the overlap reduction function of A/E channels, then the low-frequency approximation fails. We derive the exact form of overlap reduction function for A/E channels. Based on the overlap reduction function, we calculate the sensitivity curves of TianQin, TianQin I+II and TianQin + LISA. We conclude that the detection sensitivity calculated with A/E channels is mostly consistent with that obtained from the equal-arm Michelson channels.

I. INTRODUCTION

A stochastic gravitational-wave (GW) background (SGWB) is formed by the incoherent superposition of plenty of unresolved GWs [1–3]. Especially, SGWB will become foreground when exceeding the detector noise level [4, 5]. The origin of SGWB can be generally divided into astrophysics and cosmology [6, 7]. The astrophysical-origin contains nearby objects, among which the Galactic double white dwarf (DWD) is predicted to produce an anisotropic foreground [8, 9]. The cosmological-origin is related to the physical processes of the early Universe, and the cosmological SGWB is generally considered to be highly isotropic unless there is a specific physical mechanism [10].

Currently, the laser interferometry is applied to detect GWs. The typical laser interferometer is equal-arm Michelson consisting of four laser links. The equal-arm Michelson has been employed for ground-based GW detectors [11, 12], where the laser noise experiences the same delays in the links and hence cancels. Unlike ground-based GW detectors, space-borne GW detectors have unequal armlengths due to the movement of satellites [13, 14]. Thus, it is hardly to construct an equal-arm Michelson for space-borne GW detectors, and the laser noise will dominate the detector noise [15]. To cancel the laser noise in the unequal-arm detectors, Tinto et.al [16, 17] proposed the time delay interferometry (TDI) technique adopting specific combinations of laser links. Among all possible TDI combinations, the TDI channel A, E and T are the most commonly used, and they form the orthogonal channel group AET. In the GW detection, A/E channels are sensitive to GWs, while

T channel works effectively for monitoring the detector noise.

Depending on whether more than one detector works at the same time, two different detection strategies are raised. One is cross-correlation method [18–21], which is applied to the scenario that multiple detectors are employed to detect a common SGWB. Under the assumption that the noise of two detectors is uncorrelated, one can distinguish the SGWB signal from the detector noise by correlating the outputs from two detectors. The other one is null-channel method [22, 23], which is proposed for a single detector. In this method, detector noise is monitored by the null channel, so that the SGWB signal can be extracted by auto-correlating the output from the detector.

When employing the above two methods to detect SGWB, the key is the auto- or cross-correlation of the detector channel. To indicate the correlation, one needs to introduce the frequency-dependent correlation coefficient of SGWB signals, i.e., overlap reduction function (ORF) [20, 21]. ORF is determined by: (i) detector orientation; (ii) detector separation, which denotes the distance between the GW measurement locations of the detector channel. For the equal-arm Michelson consisting of one laser interference site, the detector separation can be directly defined as the distance between the interference site of both equal-arm Michelsons. However, A/E channels contain multiple laser interference sites due to their construction [24], it is nontrivial to define the detector separation. Then by simplifying A/E channels to two orthogonal equal-arm Michelsons under the low-frequency approximation, Seto et al. calculated the ORF for multiple triangular detectors [25]. Splitting the TDI channel into component links, Hu et al. derived the ORF for any TDI channel without low-frequency approximation, based on which they calculated the ORF of A/E channels for TianQin + LISA [26].

* huyiming@sysu.edu.cn

ORF only involves the correlation between the detector channel, for which if one wants to demonstrate the detection capability, the detector noise level also needs to be considered. In general, detector noise level is characterized by noise power spectral density (PSD). Then based on the ORF and noise PSD, the sky-average sensitivity curve is introduced [27]. Furthermore, the improvement in sensitivity that comes from the accumulation of correlation time and integrating over frequency also should be illustrated for SGWB detection [28]. Therefore, two more appropriate sensitivity curves, namely power-law integrated sensitivity (PLIS) curve [29] and peak-integrated sensitivity (PIS) curve [30] are proposed.

This paper aims to investigate the impacts of A/E channels on SGWB detection. First, we select a reference interference site for the detector channel, then the distance between the reference interference sites can be defined as the detector separation. Following this rule, one can calculate the ORF for any channel. Next, for TianQin, TianQin I+II and TianQin + LISA, we calculate the ORFs of the equal-arm Michelson and A/E channels without low-frequency approximation, respectively. Based on the ORFs, we further draw the corresponding PLIS and PIS curves. We find that the sensitivity curve of A/E channels is basically consistent with that of the equal-arm Michelson.

The outline of this paper is as follows. In Sec. II, we introduce the strength of SGWB. The channel response to SGWB is discussed in Sec. III. The ORF is derived in Sec. IV. Sec. V and VI are applied to assess SGWB detection. Our conclusions are discussed in Sec. VII. In addition, we show the response to GW for equal-arm Michelson in Appendix A. The discussion on the ORF and noise level for channels are in Appendix B and Appendix C, respectively. The derivation for cross-correlation and null-channel methods is shown in Appendix D.

II. STRENGTH OF STOCHASTIC GRAVITATIONAL-WAVE BACKGROUND

In our work, we focus on stationary, unpolarized and Gaussian SGWB. Then the statistical properties of the SGWB can be characterized by the dimensionless energy spectral density $\Omega_{\text{gw}}(f)$, which is normalized by the critical energy density ρ_c [31]:

$$\Omega_{\text{gw}}(f) = \frac{1}{\rho_c} \frac{d\rho_{\text{gw}}}{d(\ln f)}, \quad (1)$$

where $\rho_c \equiv 3H_0^2 c^2 / (8\pi G)$ with the light speed c , the gravitational constant G , and the Hubble constant H_0 . In general, we can adopt $h_0^2 \Omega_{\text{gw}}$ rather than Ω_{gw} to remove the measurement uncertainty of H_0 , where $H_0 = h_0 \times 100 \text{ km s}^{-1} \text{ Mpc}^{-1}$. $d\rho_{\text{gw}}$ denotes the GW energy density ρ_{gw} stored in the frequency segment df , and in terms of the transverse-traceless metric perturbation

$h_{ab}(t, \vec{x})$, GW energy density can be defined as [32, 33]

$$\rho_{\text{gw}} = \frac{c^2}{32\pi G} \langle \dot{h}_{ab}(t, \vec{x}) \dot{h}^{ab}(t, \vec{x}) \rangle, \quad (2)$$

where $\langle \rangle$ indicates averaging over several wavelengths or periods of the GW.

Since the SGWB is a collection of a large number of GWs, the transverse-traceless metric perturbation of the SGWB can be expanded as a superposition of the GW with wave vector \hat{k} :

$$h_{ab}(t, \vec{x}) = \int_{-\infty}^{\infty} df \int_{S^2} d\hat{\Omega}_{\hat{k}} \tilde{h}_{ab}(f, \hat{k}) e^{i2\pi f[t - \hat{k} \cdot \vec{x}(t)/c]}, \quad (3)$$

where $h_{ab}(t, \vec{x}) = h_{ab}(t - \hat{k} \cdot \vec{x}/c, \vec{0})$. In terms of polarization modes $P = +, \times$ and polarization tensors $e_{ab}^P(\hat{k})$, the Fourier amplitude $\tilde{h}_{ab}(f, \hat{k})$ can be expressed as: $\tilde{h}_{ab}(f, \hat{k}) = \sum_{P=+, \times} \tilde{h}_P(f, \hat{k}) e_{ab}^P(\hat{k})$. The amplitude $\tilde{h}_P(f, \hat{k})$ is a random value with zero-mean, and the conjugate symmetry of Fourier transform holds: $\tilde{h}_P(f, \hat{k}) = \tilde{h}_P^*(-f, \hat{k})$.

Assuming SGWB is stationary, the PSD of SGWB in propagation direction \hat{k} can be defined by

$$\langle \tilde{h}_P(f, \hat{k}) \tilde{h}_{P'}^*(f', \hat{k}') \rangle = \frac{1}{4} \delta(f - f') \delta_{PP'} \delta^2(\hat{k} - \hat{k}') \mathcal{P}_h(f, \hat{k}), \quad (4)$$

where the factor of 1/4 agrees with the one-sided PSD and the contribution of each polarization. The PSD $\mathcal{P}_h(f, \hat{k})$ is factorized by angular distribution $\mathcal{P}_h(\hat{k})$ and spectral density $\bar{H}(f)$: $\mathcal{P}_h(f, \hat{k}) = \mathcal{P}_h(\hat{k}) \bar{H}(f)$. The spectral density can be further normalized by the reference frequency: $\bar{H}(f) = \bar{H}(f_{\text{ref}})(f/f_{\text{ref}})^\epsilon$, where the power-law index ϵ depends on the origin of SGWB [34]. For an anisotropic SGWB, angular distribution $\mathcal{P}_h(\hat{k})$ is usually decomposed into spherical harmonics [35]:

$$\mathcal{P}_h(\hat{k}) = \sum_{l=0}^{\infty} \sum_{m=-l}^l \mathcal{P}_{lm} Y_{lm}(\hat{k}). \quad (5)$$

Furthermore, the sum of \mathcal{P}_h in all directions is the one-sided strain PSD $S_h(f)$ of SGWB:

$$S_h(f) = \int_{S^2} d\hat{\Omega}_{\hat{k}} \mathcal{P}_h(f, \hat{k}), \quad (6)$$

and for an unpolarized SGWB:

$$S_h^+(f) = S_h^\times(f) = \frac{1}{2} S_h(f). \quad (7)$$

Then in terms of Eq. (3), Eq. (4) and Eq. (6), the energy density of SGWB can be calculated by

$$\begin{aligned} \rho_{\text{gw}} &= \frac{c^2}{32\pi G} \int_{-\infty}^{\infty} df \int_{-\infty}^{\infty} df' \int_{S^2} d\hat{\Omega}_{\hat{k}} \int_{S^2} d\hat{\Omega}_{\hat{k}'} \\ &\quad \times 4\pi^2 \sum_{PP'} \langle \tilde{h}_P(f, \hat{k}) \tilde{h}_{P'}^*(f', \hat{k}') \rangle e_{ab}^P(\hat{k}) e_{ab}^{P'}(\hat{k}') \\ &\quad \times e^{i2\pi[(f-f')t - (\hat{k}-\hat{k}') \cdot \vec{x}(t)/c]} \\ &= \frac{\pi c^2}{4G} \int_0^\infty df f^2 S_h(f), \end{aligned} \quad (8)$$

Combined with Eq. (1) and Eq. (8), the energy spectral density $\Omega_{\text{gw}}(f)$ can be converted to $S_h(f)$ through

$$\Omega_{\text{gw}}(f) = \frac{2\pi^2}{3H_0^2} f^3 S_h(f). \quad (9)$$

Note that in some studies, $S_h(f)$ only contains the contribution of one polarization, so the factor of 2 on the molecule of Eq. (9) turns to 4 [36].

III. CHANNEL RESPONSE TO STOCHASTIC GRAVITATIONAL-WAVE BACKGROUND

In this section, we further discuss the response of channels to SGWB on the detector. Generally speaking, the channel response to SGWB always changes due to detector motion. However, it is reasonable to assume that the response is nearly unchanged within a sufficiently short period $[t_0 - T/2, t_0 + T/2]$. Then with the help of short-term Fourier transform, the SGWB signal that is a convolution of the metric perturbation $h_{ab}(t, \vec{x})$ and the impulse response $\mathbb{D}^{ab}(t, \vec{x})$ can be expressed as [37]:

$$\begin{aligned} h(t, t_0) &= \mathbb{D}^{ab}[t, \vec{x}(t_0)] * h_{ab}[t, \vec{x}(t_0)] \\ &= \sum_{P=+, \times} \int_{-\infty}^{\infty} df \int_{S^2} d\hat{\Omega}_{\hat{k}} F^P(f, \hat{k}, t_0) \tilde{h}_P(f, \hat{k}) \\ &\quad \times e^{i2\pi f[t - \hat{k} \cdot \vec{x}(t_0)/c]}, \end{aligned} \quad (10)$$

where \vec{x} labels the location where GW measurement occurs. The response function can be decomposed as $F^P(f, \hat{k}, t_0) = e_{ab}^P(\hat{k}) F^{ab}(f, \hat{k}, t_0)$ with

$$\begin{aligned} F^{ab}(f, \hat{k}, t_0) &= \int_{t_0 - T/2}^{t_0 + T/2} d\tau \int d^3\vec{y} \mathbb{D}^{ab}[\tau, \vec{y}(t_0)] \\ &\quad \times e^{-i2\pi f[\tau - \hat{k} \cdot \vec{y}(t_0)/c]}, \end{aligned} \quad (11)$$

and the frequency domain signal is expressed as

$$\tilde{h}(f, t_0) = \int_{S^2} d\hat{\Omega}_{\hat{k}} \sum_{P=+, \times} F^P(f, \hat{k}, t_0) \tilde{h}_P(f, \hat{k}) e^{-i2\pi f \hat{k} \cdot \vec{x}(t_0)/c}. \quad (12)$$

For ground-based GW detectors [11, 12], the equal-arm Michelson can be employed to detect GWs because the armlength keeps unchanged. When it comes to spaceborne detectors [13, 14], the armlength is difficult to be maintained and the TDI channel is introduced to cancel the laser noise [22, 23, 38]. However, to facilitate the discussion for the impacts of the TDI channel A/E on SGWB detection, we will construct both the equal-arm Michelson and A/E channels in the same regular triangle detector.

As shown in Fig. 1, we can construct an equal-arm Michelson by a vertex and two adjacent edges. Following this rule, the equal-arm Michelson channel group $M_1 M_2 M_3$ can be constructed based on the corner satellite A_0 , B_0 and C_0 , respectively. In addition, by defining the

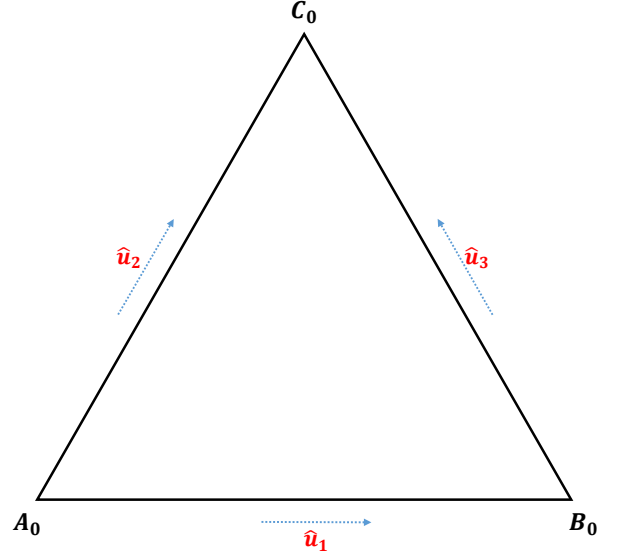


FIG. 1. Schematic diagram of a regular triangle detector.

round trip of the laser in one arm as two-way tracking, the equal-arm Michelson consists of two different two-way trackings. Then the response functions of channel group $M_1 M_2 M_3$ can be written as

$$\begin{aligned} F_{M_1}^P(f, \hat{k}, t_0) &= F_{\text{II}}^P[f, \hat{k}, \hat{u}_1(t_0)] - F_{\text{II}}^P[f, \hat{k}, \hat{u}_2(t_0)], \\ F_{M_2}^P(f, \hat{k}, t_0) &= F_{\text{II}}^P[f, \hat{k}, \hat{u}_3(t_0)] - F_{\text{II}}^P[f, \hat{k}, -\hat{u}_1(t_0)], \\ F_{M_3}^P(f, \hat{k}, t_0) &= F_{\text{II}}^P[f, \hat{k}, -\hat{u}_2(t_0)] - F_{\text{II}}^P[f, \hat{k}, -\hat{u}_3(t_0)], \end{aligned} \quad (13)$$

where F_{II}^P is the response function of the two-way tracking, and $\overrightarrow{A_0 B_0} = L\hat{u}_1$, $\overrightarrow{A_0 C_0} = L\hat{u}_2$, $\overrightarrow{B_0 C_0} = L\hat{u}_3$ with the armlength L . More details are shown in Appendix A.

In terms of the two responses of the same equal-arm Michelson with a time delay of $2L/c$, the response function of TDI Michelson X can be obtained by

$$\begin{aligned} F_X^P(f, \hat{k}, t_0) &= F_{M_1}^P(f, \hat{k}, t_0) - F_{M_1}^P(f, \hat{k}, t_0 - 2L/c) \\ &= (1 - e^{-i2f/f_*}) F_{M_1}^P(f, \hat{k}, t_0). \end{aligned} \quad (14)$$

Following the cyclic substitution, the response functions of Y and Z are

$$\begin{aligned} F_Y^P(f, \hat{k}, t_0) &= (1 - e^{-i2f/f_*}) F_{M_2}^P(f, \hat{k}, t_0), \\ F_Z^P(f, \hat{k}, t_0) &= (1 - e^{-i2f/f_*}) F_{M_3}^P(f, \hat{k}, t_0). \end{aligned} \quad (15)$$

Furthermore, the orthogonal channel group AET can be formed by channel group XYZ [24, 39, 40]:

$$\begin{aligned} A &= \frac{1}{\sqrt{2}}(Z - X), \\ E &= \frac{1}{\sqrt{6}}(X - 2Y + Z), \\ T &= \frac{1}{\sqrt{3}}(X + Y + Z). \end{aligned} \quad (16)$$

Note that, the correlation between channel X, Y and Z is not taken into account in Eq. (16). Considering this correlation, Adams et.al [41, 42] provide a new construction for channel group AET. In this work, we still adopt Eq. (16) which is more widely used.

Through the above construction, there will be multiple laser interference sites in channel A, E and T. In order to derive the response functions of channel group AET, one needs to calculate the corresponding SGWB signals based on Eq. (12):

$$\begin{aligned}
\tilde{h}_A(f, t_0) &= \frac{1}{\sqrt{2}}(\tilde{h}_Z(f, t_0) - \tilde{h}_X(f, t_0)) \\
&= \sum_{P=+, \times} \int_{S^2} d\hat{\Omega}_{\hat{k}} \frac{1}{\sqrt{2}} [F_Z^P(f, \hat{k}, t_0) e^{-i2\pi f \hat{k} \cdot \overrightarrow{OC_0}(t_0)/c} - F_X^P(f, \hat{k}, t_0) e^{-i2\pi f \hat{k} \cdot \overrightarrow{OA_0}(t_0)/c}] \tilde{h}_P(f, \hat{k}) \\
&= \sum_{P=+, \times} \int_{S^2} d\hat{\Omega}_{\hat{k}} F_A^P(f, \hat{k}, t_0) \tilde{h}_P(f, \hat{k}) e^{-i2\pi f \hat{k} \cdot \overrightarrow{OA_0}(t_0)/c}, \\
\tilde{h}_E(f, t_0) &= \frac{1}{\sqrt{6}}(\tilde{h}_X(f, t_0) - 2\tilde{h}_Y(f, t_0) + \tilde{h}_Z(f, t_0)) \\
&= \sum_{P=+, \times} \int_{S^2} d\hat{\Omega}_{\hat{k}} F_E^P(f, \hat{k}, t_0) \tilde{h}_P(f, \hat{k}) e^{-i2\pi f \hat{k} \cdot \overrightarrow{OA_0}(t_0)/c}, \\
\tilde{h}_T(f, t_0) &= \frac{1}{\sqrt{3}}(\tilde{h}_X(f, t_0) + \tilde{h}_Y(f, t_0) + \tilde{h}_Z(f, t_0)) \\
&= \sum_{P=+, \times} \int_{S^2} d\hat{\Omega}_{\hat{k}} F_T^P(f, \hat{k}, t_0) \tilde{h}_P(f, \hat{k}) e^{-i2\pi f \hat{k} \cdot \overrightarrow{OA_0}(t_0)/c}, \tag{17}
\end{aligned}$$

where the vertex A_0 is selected to the reference interference site. Then the response functions are

$$\begin{aligned}
F_A^P(f, \hat{k}, t_0) &= \frac{1}{\sqrt{2}} [F_Z^P(f, \hat{k}, t_0) e^{-i2\pi f \hat{k} \cdot \overrightarrow{A_0C_0}(t_0)/c} - F_X^P(f, \hat{k}, t_0)], \\
F_E^P(f, \hat{k}, t_0) &= \frac{1}{\sqrt{6}} [F_X^P(f, \hat{k}, t_0) - 2F_Y^P(f, \hat{k}, t_0) e^{-i2\pi f \hat{k} \cdot \overrightarrow{A_0B_0}(t_0)/c} + F_Z^P(f, \hat{k}, t_0) e^{-i2\pi f \hat{k} \cdot \overrightarrow{A_0C_0}(t_0)/c}], \\
F_T^P(f, \hat{k}, t_0) &= \frac{1}{\sqrt{3}} [F_X^P(f, \hat{k}, t_0) + F_Y^P(f, \hat{k}, t_0) e^{-i2\pi f \hat{k} \cdot \overrightarrow{A_0B_0}(t_0)/c} + F_Z^P(f, \hat{k}, t_0) e^{-i2\pi f \hat{k} \cdot \overrightarrow{A_0C_0}(t_0)/c}]. \tag{18}
\end{aligned}$$

Similarly, one can also construct channel group A'E'T' for another regular triangle detector with the response functions:

$$\begin{aligned}
F_{A'}^P(f, \hat{k}, t_0) &= \frac{1}{\sqrt{2}} [F_{Z'}^P(f, \hat{k}, t_0) e^{-i2\pi f \hat{k} \cdot \overrightarrow{A'_0C'_0}(t_0)/c} - F_{X'}^P(f, \hat{k}, t_0)], \\
F_{E'}^P(f, \hat{k}, t_0) &= \frac{1}{\sqrt{6}} [F_{X'}^P(f, \hat{k}, t_0) - 2F_{Y'}^P(f, \hat{k}, t_0) e^{-i2\pi f \hat{k} \cdot \overrightarrow{A'_0B'_0}(t_0)/c} + F_{Z'}^P(f, \hat{k}, t_0) e^{-i2\pi f \hat{k} \cdot \overrightarrow{A'_0C'_0}(t_0)/c}], \\
F_{T'}^P(f, \hat{k}, t_0) &= \frac{1}{\sqrt{3}} [F_{X'}^P(f, \hat{k}, t_0) + F_{Y'}^P(f, \hat{k}, t_0) e^{-i2\pi f \hat{k} \cdot \overrightarrow{A'_0B'_0}(t_0)/c} + F_{Z'}^P(f, \hat{k}, t_0) e^{-i2\pi f \hat{k} \cdot \overrightarrow{A'_0C'_0}(t_0)/c}], \tag{19}
\end{aligned}$$

where A'_0, B'_0, C'_0 are the vertexes, and A'_0 is the reference interference site.

For the same detector, there is no correlation between the responses of A, E, and T to SGWB, and T is the null channel where the response to SGWB is highly suppressed. More details are shown in Appendix B.

IV. OVERLAP REDUCTION FUNCTION

In order to characterize the statistical properties of SGWB signal, one can introduce the correlation PSD¹:

$$\langle \tilde{h}_I(f, t_0) \tilde{h}_J^*(f', t_0) \rangle = \frac{1}{2} \delta(f - f') P_{h_{IJ}}(f, t_0), \tag{20}$$

¹ The auto-correlation PSD P_{h_I} is a real function.

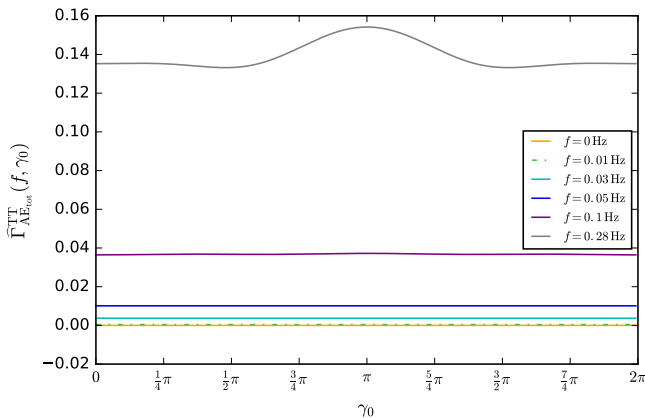


FIG. 2. Total ORF of TianQin I+II for different initial angle difference γ_0 .

where

$$P_{h_{IJ}}(f, t_0) = \Upsilon_{IJ}(f, t_0) S_h(f). \quad (21)$$

Then we can connect the PSDs of SGWB and SGWB signal through the universal ORF Υ_{IJ} , which is independent of SGWB spectral density $\bar{H}(f)$:

$$\Upsilon_{IJ}(f, t_0) = \frac{\int_{S^2} d\hat{\Omega}_{\hat{k}} \mathcal{Y}_{IJ}(f, \hat{k}, t_0) \mathcal{P}_h(\hat{k})}{\int_{S^2} d\hat{\Omega}_{\hat{k}} \mathcal{P}_h(\hat{k})}. \quad (22)$$

The geometric factor specifies the correlation between the responses of channel I and J to SGWB:

$$\mathcal{Y}_{IJ}(f, \hat{k}, t_0) = \frac{1}{2} \sum_{P=+, \times} F_I^P(f, \hat{k}, t_0) F_J^{P*}(f, \hat{k}, t_0) \times e^{-i2\pi f \hat{k} \cdot [\vec{x}_I(t_0) - \vec{x}_J(t_0)]/c}, \quad (23)$$

where $\vec{x}_{I,J}$ denotes the laser interference sites of channel I and J .

For an isotropic SGWB, the universal ORF turns to the classical ORF:

$$\Gamma_{IJ}(f, t_0) = \frac{1}{4\pi} \int_{S^2} d\hat{\Omega}_{\hat{k}} \mathcal{Y}_{IJ}(f, \hat{k}, t_0). \quad (24)$$

For the case of the channel A and A' mentioned above, the ORF

$$\Gamma_{AA'}(f, t_0) = \frac{1}{8\pi} \sum_{P=+, \times} \int_{S^2} d\hat{\Omega}_{\hat{k}} F_A^P(f, \hat{k}, t_0) F_{A'}^{P*}(f, \hat{k}, t_0) \times e^{-i2\pi f \hat{k} \cdot \overrightarrow{A'_0 A_0}(t_0)/c}, \quad (25)$$

where $A'_0 A_0$ denotes the detector separation. Especially, the ORF of one channel reduces to the transfer function $\mathcal{R}(f)$. In the situation that ORF changes over time, we need to further define the time-averaged ORF for the total correlation time T_{tot} [43]:

$$\bar{\Gamma}_{IJ}(f) = \sqrt{\frac{1}{T_{\text{tot}}} \int_0^{T_{\text{tot}}} dt |\hat{\Gamma}_{IJ}(f, t_0)|^2}. \quad (26)$$

For TianQin I+II and TianQin + LISA, one can construct four pairs of channels for cross-correlation detection, then the *total* ORF of TianQin I+II and TianQin + LISA is defined as [25]

$$\Gamma_{IJ_{\text{tot}}}(f) = \sqrt{\sum_{I,J} |\bar{\Gamma}_{IJ}(f)|^2}, \quad (27)$$

where I and J label a pair of orthogonal equal-arm Michelsons or A/E channels, i.e., $\Gamma_{\text{MM}_{\text{tot}}}$ or $\Gamma_{\text{AE}_{\text{tot}}}$. Next, we will demonstrate the calculation of the ORF for TianQin I+II and TianQin + LISA, respectively. And as a shorthand label, we might employ TQ for TianQin, TT for TianQin I+II, TL for TianQin + LISA in the figures and equations.

For TianQin I+II, since the orbital planes of TianQin and TianQin II will be perpendicular to each other all the time, the total ORF will not change over time under the low-frequency approximation [25]. However, if low-frequency approximation fails, the total ORF will be affected by the launch times of two detectors, i.e., the initial angles of TianQin and TianQin II [43]. We denote the initial angular difference between TianQin and TianQin II with γ_0 , and show the total ORF of A/E channels within one orbital period of TianQin in Fig. 2. We find that the optimal ORF will be obtained when $\gamma_0 = (2n+1)\pi$ with $n = 0, 1, 2, \dots$, i.e., the launch time difference between TianQin and TianQin II should be set to the semi-integer multiple of the orbital period. However, our previous work concluded that for the equal-arm Michelson, the launch time difference should be an integer multiple of the orbital period². Note that, there must be an overlap in the operation periods of TianQin and TianQin II, or the correlation time will drop to 0. Because the nominal working mode of TianQin is set to “three months on + three months off”, one needs to extend the operating time so that TianQin and TianQin II will run simultaneously for sufficient time.

As for TianQin + LISA, the angle between the orbital planes of TianQin and LISA will change periodically in a cycle of about one year [43]. Besides, under the premise of LISA operating throughout the year, the TianQin + LISA configuration can perform cross-correlation detection only when TianQin is running. In terms of the nominal working mode of TianQin, we show the ORF of TianQin + LISA throughout one year with low-frequency approximation in Fig. 3. The top and bottom panels are the results of the equal-arm Michelson and A/E channels, respectively, where the dashed part indicates that TianQin is off duty. Meanwhile, we mark the perihelion with blue dot³. The primary and secondary peaks of both ORFs occur at $t = 0.176, 0.676$ yr, on which TianQin is off.

² It is shown in Fig. 4 of Ref. [43].

³ For the equal-arm Michelson, one can set $f = 0$ Hz to get the ORF under the low-frequency approximation; but for A/E channels, the ORF drops to 0 when $f = 0$ Hz, so we set $f = 10^{-5}$ Hz.

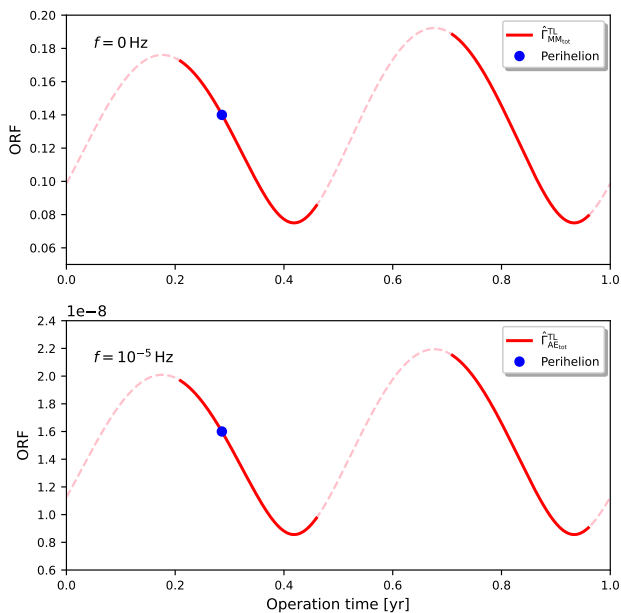


FIG. 3. ORFs of the equal-arm Michelson (top panel) and A/E channels (bottom panel) for TianQin + LISA.

Furthermore, since the orbital period of LISA is about 100 times that of TianQin, regardless of the initial angle of TianQin, the total ORF of TianQin + LISA will not change after one year of cross-correlation detection.

Based on the above analysis, the total ORFs of TianQin I+II and TianQin + LISA are shown in Fig. 4, where the transfer function of TianQin is also involved for comparison. Similar to the transfer function, the ORF of equal-arm Michelson remains constant with low-frequency approximation, while for A/E channels it is proportional to f^2 .

V. DETECTION METHOD

The output $s(t)$ of detector channel mainly contains SGWB signal $h(t)$ and channel noise $n(t)$. Unless the SGWB signal is much larger in magnitude than the channel noise, it is almost impossible to separate the signal from the noise through a single-channel measurement [28]. The general strategies are cross-correlating the outputs from different noise-independent channels [18, 20, 21] and auto-correlating the output from one channel under the noise monitoring of the null channel [37, 44].

In cross-correlation method, one can define the product of two outputs as the correlator, then the measurement

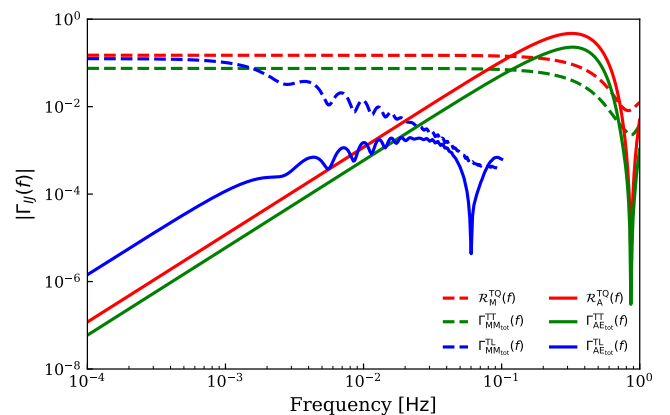


FIG. 4. Transfer function and ORF for different detector configurations. Red, green and blue lines match TianQin, TianQin I+II and TianQin + LISA, while dashed and solid lines denote the results of the equal-arm Michelson and A/E channels, respectively. Due to the limitation of calculation accuracy, the ORF for TianQin + LISA is truncated to 0.1 Hz.

can be obtained by integrating the correlator over time:

$$\begin{aligned}
 S_{IJ}(t_0) &= \int_{t_0-T/2}^{t_0+T/2} dt \int_{t_0-T/2}^{t_0+T/2} dt' s_I(t) s_J(t') Q_{IJ}(t-t', t_0) \\
 &\approx \int_{t_0-T/2}^{t_0+T/2} dt \int_{-\infty}^{\infty} df \int_{-\infty}^{\infty} df' \tilde{s}_I(f, t_0) \tilde{s}_J^*(f', t_0) \\
 &\quad \times \frac{P_{h_{IJ}}^*(f, t_0)}{P_{n_I}(f) P_{n_J}(f) W_{IJ}(f, t_0)} e^{-i2\pi(f-f')t}, \quad (28)
 \end{aligned}$$

where P_n is the noise PSD, and the correction function

$$\begin{aligned}
 W_{IJ}(f, t_0) &= 1 + \frac{P_{h_I}(f, t_0) P_{n_J}(f) + P_{h_J}(f, t_0) P_{n_I}(f)}{P_{n_I}(f) P_{n_J}(f)} \\
 &\quad + \frac{P_{h_I}(f, t_0) P_{h_J}(f, t_0) + |P_{h_{IJ}}(f, t_0)|^2}{P_{n_I}(f) P_{n_J}(f)}. \quad (29)
 \end{aligned}$$

Under the assumption that SGWB signal and channel noise are stationary in the time interval $[t_0 - T/2, t_0 + T/2]$, the filter function $Q_{IJ}(t, t') = Q_{IJ}(t - t')$.

In terms of the expectation value and variance of the measurement

$$\begin{aligned}
 \mu(t_0) &= \langle S_{IJ}(t_0) \rangle, \\
 \sigma^2(t_0) &= \langle S_{IJ}(t_0) S_{IJ}(\eta_0) \rangle - \langle S_{IJ}(t_0) \rangle \langle S_{IJ}(\eta_0) \rangle, \quad (30)
 \end{aligned}$$

the signal-to-noise ratio (SNR) can be obtained by

$$\rho(t_0) = \frac{\mu(t_0)}{\sigma(t_0)} = \sqrt{2T \int_{f_{\min}}^{f_{\max}} df \frac{|P_{h_{IJ}}(f, t_0)|^2}{P_{n_I}(f) P_{n_J}(f) W_{IJ}(f, t_0)}}. \quad (31)$$

For a single TianQin-like detector, the correlation between the SGWB signal of noise-independent channels cancels [41, 45]. Thus the cross-correlation method will fail, and the null-channel method need to be introduced.

For the channel group A/E, one can construct the correlator for null-channel method by

$$s_0(t, t') = \sum_{I=A,E} \left[s_I(t) s_I(t') - \frac{1}{2} \int_{-\infty}^{\infty} df e^{i2\pi f(t-t')} P_{n_I}(f) \right], \quad (32)$$

$$\begin{aligned} K(t_0) &= \int_{t_0-T/2}^{t_0+T/2} dt \int_{t_0-T/2}^{t_0+T/2} dt' s_0(t, t') Q_{II}(t-t', t_0) \\ &\approx \sum_{I=A,E} \int_{t_0-T/2}^{t_0+T/2} dt \int_{-\infty}^{\infty} df \int_{-\infty}^{\infty} df' \left[\tilde{s}_I(f, t_0) \tilde{s}_I^*(f', t_0) - \frac{1}{2} P_{n_I}(f) \right] \frac{P_{h_I}(f, t_0) e^{-i2\pi(f-f')t_0}}{P_{n_I}^2(f) W_I(f, t_0)}, \end{aligned} \quad (33)$$

where the correction function

$$W_I(f, t_0) = \left(1 + \frac{P_{h_I}(f, t_0)}{P_{n_I}(f)} \right)^2. \quad (34)$$

For a symmetric scenario, one can further assume

$$\begin{aligned} P_{h_A}(f, t_0) &= P_{h_E}(f, t_0), \\ P_{n_A}(f) &= P_{n_E}(f). \end{aligned} \quad (35)$$

Then the SNR of null-channel method is given by

$$\begin{aligned} \rho(t_0) &= \frac{\langle K(t_0) \rangle}{\sqrt{\langle K(t_0) K(\eta_0) \rangle - \langle K(t_0) \rangle \langle K(\eta_0) \rangle}} \\ &= \sqrt{2T \int_{f_{\min}}^{f_{\max}} df \frac{P_{h_I}^2(f, t_0)}{P_{n_I}^2(f) W_I(f, t_0)}}. \end{aligned} \quad (36)$$

By setting $I = J$, the SNR of cross-correlation method (i.e., Eq. (31)) returns to that of null-channel method (i.e., Eq. (36)). More details are shown in Appendix D.

As the SNR is proportional to \sqrt{T} , we can accumulate a sufficiently high SNR by correlating plenty of data sets. For the total correlation time $T_{\text{tot}} = nT$, the SNR

$$\begin{aligned} \rho &= \sqrt{\sum_{t_0=0}^{(n-1)T} \rho^2(t_0)} \\ &= \sqrt{2T \int_{f_{\min}}^{f_{\max}} df \sum_{t_0=0}^{(n-1)T} \frac{|P_{h_{IJ}}(f, t_0)|^2}{P_{n_I}(f) P_{n_J}(f) W_{IJ}(f, t_0)}}. \end{aligned} \quad (37)$$

When SGWB signal is much stronger than channel noise, the total SNR

$$\begin{aligned} \rho &= \sqrt{2T \int_{f_{\min}}^{f_{\max}} df \sum_{t_0=0}^{(n-1)T} \frac{1}{\frac{P_{h_I}(f, t_0) P_{h_J}(f, t_0)}{|P_{h_{IJ}}(f, t_0)|^2} + (1 - \delta_{IJ})}} \\ &\leq \sqrt{(1 + \delta_{IJ}) T_{\text{tot}} (f_{\max} - f_{\min})}, \end{aligned} \quad (38)$$

where $|P_{h_{IJ}}(f, t_0)|^2 \leq P_{h_I}(f, t_0) P_{h_J}(f, t_0)$. We can find that the SNR is limited to a certain value, which is determined by three factors: (i) the type of detection method;

where the noise PSD of A/E channels can be monitored by the null channel T. Similar to Eq. (28), we can obtain the measurement by

(ii) the correlation time T_{tot} ; (iii) detection frequency band $[f_{\min}, f_{\max}]$. On the contrary, when SGWB is much weaker than channel noise, the correction function $W_{IJ}(f, t_0) \rightarrow 1$. In this case, the SNR for an isotropic SGWB can be simplified to the following form:

$$\rho = \sqrt{2T_{\text{tot}} \int_{f_{\min}}^{f_{\max}} df \frac{[\bar{\Gamma}_{IJ}(f) S_h(f)]^2}{P_{n_I}(f) P_{n_J}(f)}}. \quad (39)$$

When SNR exceeds the preset threshold, the SGWB detection will be announced.

As for the SNR threshold, the preliminary result is provided by Ref. [28]:

$$\rho_{\text{thr}} = \sqrt{2} [\text{erfc}^{-1}(2\alpha) - \text{erfc}^{-1}(2\gamma)], \quad (40)$$

where the false alarm rate α and the detection rate γ are set in advance. For example, when choosing $\alpha = 0.1$ and $\gamma = 0.9$, the SNR threshold $\rho_{\text{thr}} = 2.56$; or $\rho_{\text{thr}} = 3.30$ with $\alpha = 0.05$ and $\gamma = 0.95$. Because the lower false alarm rate and the higher detection rate imply that the detector is more sensitive to GWs, the higher SNR threshold is required.

VI. SENSITIVITY CURVE

We can further demonstrate the detection capability of the detector through the sensitivity curve. The *sky-averaged* sensitivity curve can be directly obtained based on the response to SGWB and noise lever of the channel [36]:

$$S_{n_I}(f) = \frac{P_{n_I}(f)}{\mathcal{R}_I(f)}, \quad (41)$$

which is applied to an isotropic SGWB.

As for two channels, the effective sensitivity curve is defined as [29]

$$S_{n_{IJ}}(f) = \frac{\sqrt{P_{n_I}(f) P_{n_J}(f)}}{\bar{\Gamma}_{IJ}(f)}, \quad (42)$$

which reduces to Eq. (41) when $I = J$. Then, Eq. (39) can be further simplified:

$$\rho = \sqrt{2T_{\text{tot}} \int_{f_{\text{min}}}^{f_{\text{max}}} df \left[\frac{S_h(f)}{S_{n_{IJ}}(f)} \right]^2}. \quad (43)$$

Meanwhile, the corresponding energy spectral density $\Omega_{n_{IJ}}$ can be converted to $S_{n_{IJ}}$ through

$$\Omega_{n_{IJ}}(f) = \frac{2\pi^2}{3H_0^2} f^3 S_{n_{IJ}}(f). \quad (44)$$

As mentioned above, the correlation time and frequency band of the detector have a significant impact on SGWB detection. Therefore, Thrane et.al [29] proposed the PLIS curve, which is applied to the power-law SGWB with the following form:

$$\Omega_{\text{gw}}(f) = \Omega_0(\epsilon)(f/f_{\text{ref}})^\epsilon|_{\epsilon=\epsilon_0}, \quad (45)$$

where Ω_0 is related to the index ϵ , and the reference frequency f_{ref} is arbitrary.

By combining Eq. (43)-Eq. (45),

$$\Omega_0(\epsilon) = \rho_{\text{thr}} \left[2T_{\text{tot}} \int_{f_{\text{min}}}^{f_{\text{max}}} df \frac{(f/f_{\text{ref}})^{2\epsilon}}{\Omega_{n_{IJ}}^2(f)} \right]^{-1/2}, \quad (46)$$

where the SNR is set to threshold ρ_{thr} . For each frequency, we can obtain the maximum Ω_{gw} with a specific index ϵ to generate the PLIS curve:

$$\Omega_{\text{PLIS}}(f) = \max_{\epsilon} [\Omega_0(\epsilon)(f/f_{\text{ref}})^\epsilon]. \quad (47)$$

The PLIS curve (on the log-log plot) specifies the envelope of power-law SGWBs, of which the SNR is equal to the preset SNR threshold. Once a power-law SGWB spectrum is somewhere above the PLIS curve, the SGWB is expected to be detected, and vice versa. It is explicit to determine whether the SGWB can be detected by the detector configuration.

We show the PLIS curves of TianQin, TianQin I+II, TianQin + LISA in Fig. 5. The solid and dashed lines are the results for the equal-arm Michelson and A/E channels, and both of them basically coincide. The result implies that when A/E channels are employed instead of the equal-arm Michelson, the detection capability of the detector configuration is nearly unchanged.

The spectrum of astrophysical SGWB is usually in power-law form, which is not true for the cosmological SGWB, such as the first-order phase transition (PT). Therefore, Schmitz et.al [30] proposed the PIS curve.

The energy spectral density of the first-order PT is expressed as

$$\Omega_{\text{gw}}(f) = \Omega_{\text{gw}}^{\text{peak}}(\{p_i\})S(f, f_{\text{peak}}), \quad (48)$$

where $\Omega_{\text{gw}}^{\text{peak}}(\{p_i\})$ is the peak amplitude at the peak frequency f_{peak} , the spectral function $S(f, f_{\text{peak}})$ depends

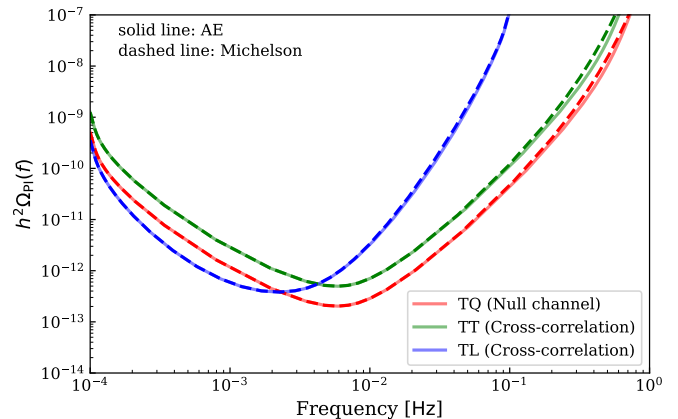


FIG. 5. PL sensitivity curves for different detector configurations. We set the SNR threshold to 3.30 and consider that during the one-year operating time, the correlation time of TianQin and TianQin + LISA is half a year, compared to four months for TianQin I+II.

on the cosmological model. Then through the definition of PIS curve

$$\Omega_{\text{PIS}}(f_{\text{peak}}) = \left[2T_{\text{tot}} \int_{f_{\text{min}}}^{f_{\text{max}}} df \left(\frac{S(f, f_{\text{peak}})}{\Omega_{n_{IJ}}(f)} \right)^2 \right]^{-1/2}, \quad (49)$$

the SNR can be obtained by

$$\rho = \frac{\Omega_{\text{gw}}^{\text{peak}}(\{p_i\})}{\Omega_{\text{PIS}}(f_{\text{peak}})}. \quad (50)$$

Once selecting a specific parameter group $\{p_i\}$, the peak frequency f_{peak} and peak amplitude $\Omega_{\text{gw}}^{\text{peak}}$ are fixed. If the peak amplitude is above ρ_{thr} times of the PIS curve, the detection of cosmological PT will be claimed.

In Fig. 6, we show the PIS curves for a certain spectral function:

$$S(f, f_{\text{peak}}) = \frac{3.8(f/f_{\text{peak}})^{2.9}}{1 + 2.9(f/f_{\text{peak}})^{3.8}}. \quad (51)$$

Similar to the PLIS curve, the PIS curves of equal-arm and A/E channels are mostly the same.

So far, this paper has discussed three types of sensitivity curves. Sky-averaged sensitivity curve is independent of correlation time and detection frequency band, and by considering the impact of the two factors on SGWB detection, PLIS curve and PIS curve are proposed. It is straightforward to determine whether SGWB can be detected by the last two sensitivity curves. Besides, the PLIS curve works for the power-law SGWB, and the PLIS curve is applied to the SGWB with pre-known spectrum.

VII. CONCLUSION

In this work, we have analyzed the impacts of A/E channels on SGWB detection for space-borne detectors.

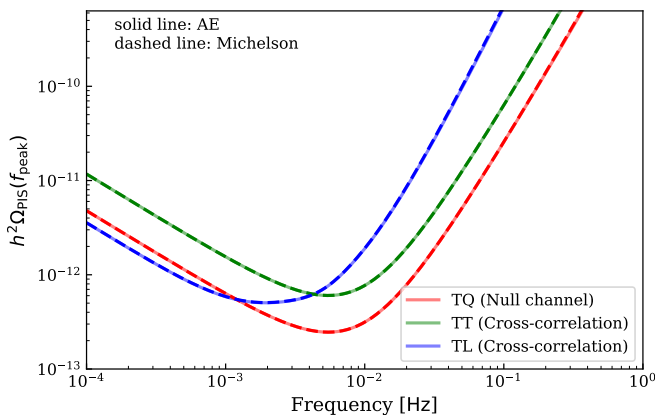


FIG. 6. PIS curves of TianQin (red), TianQin I+II (green) and TianQin +LISA (blue) for A/E channels (solid line) and equal-arm Michelson (dashed line). The setting of the correlation time for the configuration is the same as when plotting the PLIS curve.

We first selected the reference interference site for A/E channels consisting multiple interference sites. In this way, it is clear to define the detector separation through the distance between reference interference sites, which works well for any channel. By means of the reference interference site, we derived the ORF that is valid across all frequency bands. For TianQin, TianQin I+II and TianQin + LISA, we calculated the ORFs for the equal-arm Michelson and A/E channels, respectively. In addition to ORF, the noise level, correlation time and frequency band of the detector also need to be folded into detection sensitivity, according to which we plotted the corresponding sensitivity curves to assess the detection capabilities.

In a certain detector configuration, the ORF and noise PSD of A/E channels differ from those of the equal-arm Michelson, but their differences share the same coefficient $6 \sin^2(f/f_*)$ under the low-frequency approximation. Since the detection sensitivity is determined by the ratio of ORF and noise PSD, the detection sensitivity of the A/E channels and the equal-arm Michelson are basically the same. We have shown that the differ-

ence between A/E channels and the equal-arm Michelson stems from the extra phase related to the position difference. For the low-frequency approximation to be valid, the wavelength of the GW should be longer than the armlength, which makes the extra phase negligible.

However, the configuration design can affect the correlation between detectors. In order to obtain optimal ORF, the configuration design is well worth a discussion. Meanwhile, the constructions of equal-arm Michelson and A/E channels are different. Therefore, the configuration design corresponding to the optimal ORF for A/E channels may differ from that for the equal-arm Michelson. TianQin I+II is one such configuration, where the launch time difference between TianQin and TianQin II is the key factor of configuration design. If one expects the optimal ORF of TianQin I+II in SGWB detection, then the launch time difference should be set to an integer and a semi-integer multiple of the orbital period for the equal-arm Michelson and A/E channels, respectively.

Recently, Bartolo et al. [46] reviewed the sensitivity curve for the detection of the anisotropic SGWB by a single LISA. Unlike for the isotropic SGWB, where only the A/E channels and the equal-arm Michelson contribute to the detection sensitivity, for the anisotropic SGWB the null channel T also has a non-negligible impact on the sensitivity. Therefore, if only considering the A/E channels and the equal-arm Michelson, the detection sensitivities for the anisotropic SGWB are different. However, by incorporating the null channel, the detection sensitivities for A/E and T, as well as the equal-arm Michelson and T for the anisotropic SGWB will be equivalent.

ACKNOWLEDGMENTS

This work has been supported by the Guangdong Major Project of Basic and Applied Basic Research (Grant No. 2019B030302001), the National Key Research and Development Program of China (No. 2020YFC2201400), the Natural Science Foundation of China (Grants No. 12173104), and the Natural Science Foundation of Guangdong Province of China (Grant No. 2022A1515011862). We also thank Shun-Jia Huang, Xiang-Yu Lyu, Jianwei Mei for helpful discussions.

Appendix A: Response to Gravitational-wave for equal-arm Michelson

In Fig. 7, \vec{r}_I and \vec{r}_{II} label the position vectors of test mass m_I and m_{II} , respectively. L is armlength and \hat{u} denotes the unit vector of the one-way tracking. At the moment t_0 , the GW signal of one-way tracking can be expressed as [37, 47]

$$h_I(t, t_0) = \frac{\delta L(t_0)}{L} = \frac{1}{L} \int_0^L ds \frac{u^a(t_0) u^b(t_0)}{2} h_{ab}[t(s), \vec{x}(s)], \quad (\text{A1})$$

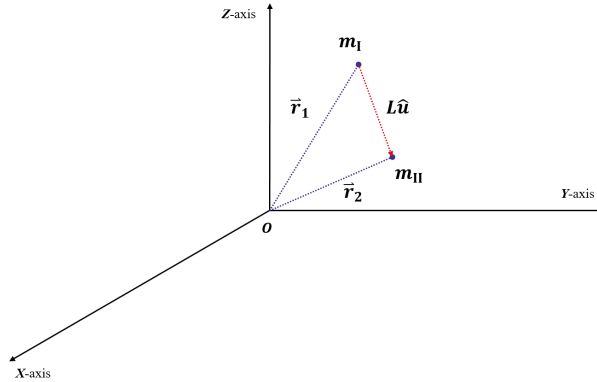


FIG. 7. Schematic diagram of the one-way tracking.

where s is the actual path of photon, and under the 0th-order approximation:

$$\begin{aligned} t(s) &= (t_0 - L/c) + s/c, \\ \vec{x}(s) &= \vec{r}_1 + s\hat{u}. \end{aligned} \quad (\text{A2})$$

In terms of Eq. (3), the one-way tracking signal of SGWB is a collection of GW signals from all directions:

$$\begin{aligned} h_{\text{I}}(t, t_0) &= \frac{1}{L} \int_{-\infty}^{\infty} df \int_{S^2} d\hat{\Omega}_{\hat{k}} \frac{u^a(t_0)u^b(t_0)}{2} h_{ab}(f, \hat{k}) e^{i2\pi f [t - \frac{L + \hat{k} \cdot (\vec{r}_2 - L\hat{u})}{c}]} \frac{c \cdot e^{-\frac{i2\pi f s}{c} (\hat{k} \cdot \hat{u}(t_0) - 1)}}{-i2\pi f (\hat{k} \cdot \hat{u}(t_0) - 1)} \Big|_{s=0}^{s=L} \\ &= \int_{-\infty}^{\infty} df \int_{S^2} d\hat{\Omega}_{\hat{k}} F_{\text{I}}^{ab}(f, \hat{k}, t_0) h_{ab}(f, \hat{k}) e^{i2\pi f (t - \frac{\hat{k} \cdot \vec{r}_2}{c})}, \end{aligned}$$

then the frequency domain signal

$$h_{\text{I}}(f, t_0) = \int_{S^2} d\hat{\Omega}_{\hat{k}} F_{\text{I}}^{ab}(f, \hat{k}, t_0) h_{ab}(f, \hat{k}) e^{-i2\pi f \hat{k} \cdot \vec{r}_2 / c}. \quad (\text{A3})$$

In Eq. (A3), the one-way tracking response function

$$F_{\text{I}}^{ab}(f, \hat{k}, t_0) = \frac{u^a(t_0)u^b(t_0)}{2} \mathcal{T}_{\text{I}}(f, \hat{k}, t_0) \quad (\text{A4})$$

and the strain transfer function

$$\mathcal{T}_{\text{I}}(f, \hat{k}, t_0) = \text{sinc}\left[\frac{f}{2f_*} [1 - \hat{k} \cdot \hat{u}(t_0)]\right] e^{-i\frac{f}{2f_*} [1 - \hat{k} \cdot \hat{u}(t_0)]} \quad (\text{A5})$$

with the characteristic frequency $f_* = c/(2\pi L)$.

For the two-way tracking where the photon returns to m_{I} after a one-way tracking, the SGWB signal

$$\begin{aligned} h_{\text{II}}(t, t_0) &= \frac{1}{2L} \int_0^L ds \frac{u^a(t_0)u^b(t_0)}{2} \left[h_{ab}\left(t - \frac{2L + \hat{k} \cdot \vec{r}_1 + [\hat{k} \cdot \hat{u}(t_0) - 1]s}{c}\right) + h_{ab}\left(t - \frac{L + \hat{k} \cdot \vec{r}_2 + [\hat{k} \cdot \hat{u}(t_0) - 1]s}{c}\right) \right] \\ &= \int_{-\infty}^{\infty} df F_{\text{II}}^{ab}(f, \hat{k}, t_0) h_{ab}(f, \hat{k}) e^{i2\pi f (t - \frac{\hat{k} \cdot \vec{r}_1}{c})}. \end{aligned} \quad (\text{A6})$$

Note that in the above formula, the length of links is assumed to not change over time.

Then the corresponding frequency domain signal

$$h_{\text{II}}(f, t_0) = \int_{-\infty}^{\infty} df F_{\text{II}}^{ab}(f, \hat{k}, t_0) h_{ab}(f, \hat{k}) e^{-i2\pi f \hat{k} \cdot \vec{r}_1 / c}, \quad (\text{A7})$$

where the response function

$$F_{\text{II}}^{ab}(f, \hat{k}, t_0) = \frac{1}{2} \mathcal{T}_{\text{II}}(f, \hat{k}, t_0) u^a(t_0) u^b(t_0) \quad (\text{A8})$$

with the strain transfer function

$$\mathcal{T}_{\text{II}}(f, \hat{k}, t_0) = \frac{1}{2} \left[\text{sinc} \left[\frac{f}{2f_*} (1 - \hat{k} \cdot \hat{u}(t_0)) \right] e^{-i \frac{f}{2f_*} [3 + \hat{k} \cdot \hat{u}(t_0)]} + \text{sinc} \left[\frac{f}{2f_*} (1 + \hat{k} \cdot \hat{u}(t_0)) \right] e^{-i \frac{f}{2f_*} [1 + \hat{k} \cdot \hat{u}(t_0)]} \right]. \quad (\text{A9})$$

For the record, the phase terms in Eq. (A3) and Eq. (A7) are related to the GW measurement location.

Since the equal-arm Michelson consists of two different two-way trackings, the response function can be written as

$$F_{\text{M}}^{ab}(f, \hat{k}, t_0) = F_{\text{II}}^{ab}(f, \hat{k}, \hat{u}(t_0)) - F_{\text{II}}^{ab}[f, \hat{k}, \hat{v}(t_0)], \quad (\text{A10})$$

where \hat{u} and \hat{v} are the unit vectors of the arms. Under the low-frequency approximation, the response function

$$F_{\text{M}}^{ab}(f, \hat{k}, t_0) = \frac{1}{2} [u^a(t_0)u^b(t_0) - v^a(t_0)v^b(t_0)]. \quad (\text{A11})$$

Appendix B: ORF of channel group

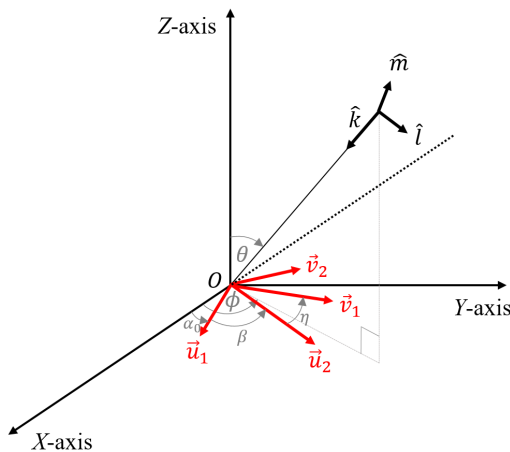


FIG. 8. Detector coordinate

As shown in Fig. 8, we can construct a set of orthogonal bases:

$$\hat{k} = (-\sin \theta \cos \phi, -\sin \theta \sin \phi, -\cos \theta), \quad (\text{B1})$$

$$\hat{l} = (\cos \theta \cos \phi, \cos \theta \sin \phi, -\sin \theta), \quad (\text{B2})$$

$$\hat{m} = (\sin \phi, -\cos \phi, 0), \quad (\text{B3})$$

where \hat{k} is the propagation direction of the GW, and \hat{m} is perpendicular to Z -axis.

In terms of \hat{l} and \hat{m} , we can further construct the polarization tensor:

$$e_{ij}^+(\hat{n}) = \hat{l}_i \hat{l}_j - \hat{m}_i \hat{m}_j, \quad (\text{B4})$$

$$e_{ij}^\times(\hat{n}) = \hat{l}_i \hat{m}_j + \hat{l}_j \hat{m}_i. \quad (\text{B5})$$

Then the analytical expression of the polarization tensor can be obtained:

$$e^+(\hat{k}) = \begin{bmatrix} \cos^2 \theta \cos^2 \phi - \sin^2 \phi & \frac{1}{2} \sin 2\phi (1 + \cos^2 \theta) & -\frac{1}{2} \sin 2\theta \cos \phi \\ \frac{1}{2} \sin 2\phi (1 + \cos^2 \theta) & \sin^2 \phi \cos^2 \theta - \cos^2 \phi & -\frac{1}{2} \sin 2\theta \sin \phi \\ -\frac{1}{2} \sin 2\theta \cos \phi & -\frac{1}{2} \sin 2\theta \sin \phi & \sin^2 \theta \end{bmatrix},$$

$$e^\times(\hat{k}) = \begin{bmatrix} \sin 2\phi \cos \theta & -\cos 2\phi \cos \theta & -\sin \phi \sin \theta \\ -\cos 2\phi \cos \theta & -\sin 2\phi \cos \theta & \cos \phi \sin \theta \\ -\sin \phi \sin \theta & \cos \phi \sin \theta & 0 \end{bmatrix}. \quad (\text{B6})$$

On the X - Y plane, we place two equal-arm Michelson channels with opening angle β between arms. The unit arm vectors of the first one M_1

$$\begin{aligned}\hat{u}_1 &= [\cos \alpha_0, \sin \alpha_0, 0], \\ \hat{u}_2 &= [\cos(\alpha_0 + \beta), \sin(\alpha_0 + \beta), 0],\end{aligned}\quad (\text{B7})$$

and of the second one M_2

$$\begin{aligned}\vec{v}_1 &= [\cos(\alpha_0 + \beta + \eta), \sin(\alpha_0 + \beta + \eta), 0] \\ \vec{v}_2 &= [\cos(\alpha_0 + 2\beta + \eta), \sin(\alpha_0 + 2\beta + \eta), 0].\end{aligned}\quad (\text{B8})$$

Without loss of generality, one can set $\alpha_0 = 0$ to simplify the calculation, and under the low-frequency approximate,

$$\begin{aligned}F_{M_1} &= \frac{1}{2}(u_1 \otimes u_1 - u_2 \otimes u_2) = \frac{\sin \beta}{2} \begin{bmatrix} \sin \beta & -\cos \beta & 0 \\ -\cos \beta & -\sin \beta & 0 \\ 0 & 0 & 0 \end{bmatrix}, \\ F_{M_2} &= \frac{1}{2}(v_1 \otimes v_1 - v_2 \otimes v_2) = \frac{\sin \beta}{2} \begin{bmatrix} \sin(3\beta + 2\eta) & -\cos(3\beta + 2\eta) & 0 \\ -\cos(3\beta + 2\eta) & -\sin(3\beta + 2\eta) & 0 \\ 0 & 0 & 0 \end{bmatrix}.\end{aligned}\quad (\text{B9})$$

Then through

$$\begin{aligned}F_{M_1}^+(0, \hat{k}) &= F_{M_1}^{ab} e_{ab}^+(\hat{k}) = \frac{3 + \cos 2\theta}{4} \sin \beta \sin(\beta - 2\phi), \\ F_{M_1}^\times(0, \hat{k}) &= F_{M_1}^{ab} e_{ab}^\times(\hat{k}) = \sin \beta \cos \theta \cos(\beta - 2\phi), \\ F_{M_2}^+(0, \hat{k}) &= F_{M_2}^{ab} e_{ab}^+(\hat{k}) = \frac{3 + \cos 2\theta}{4} \sin \beta \sin(3\beta + 2\eta - 2\phi), \\ F_{M_2}^\times(0, \hat{k}) &= F_{M_2}^{ab} e_{ab}^\times(\hat{k}) = \sin \beta \cos \theta \cos(3\beta + 2\eta - 2\phi),\end{aligned}\quad (\text{B10})$$

we can calculate the transfer function and ORF:

$$\begin{aligned}\mathcal{R}_{M_1}(0) &= \frac{1}{8\pi} \sum_{P=+, \times} \int_{S^2} d\hat{\Omega}_k F_{M_1}^P(0, \hat{k}) F_{M_1}^{P*}(0, \hat{k}) = \frac{\sin^2 \beta}{5} = \mathcal{R}_{M_2}(0), \\ \Gamma_{M_{12}}(0) &= \frac{1}{8\pi} \sum_{P=+, \times} \int_{S^2} d\hat{\Omega}_k F_{M_1}^P(0, \hat{k}) F_{M_2}^{P*}(0, \hat{k}) = \frac{\sin^2 \beta \cos[2(\beta + \eta)]}{5}.\end{aligned}\quad (\text{B11})$$

For the equal-arm Michelson channels built in TianQin, $\beta = \pi/3$ and $\beta + \eta = 2\pi/3$, then

$$\mathcal{R}_{M_1}(0) = -2\Gamma_{M_{12}}(0).\quad (\text{B12})$$

In terms of Eq. (14) and Eq. (15),

$$\lim_{f \rightarrow 0} \frac{\mathcal{R}_X(f)}{\Gamma_{XY}(f)} = \lim_{f \rightarrow 0} \frac{\mathcal{R}_{M_1}(f)}{\Gamma_{M_{12}}(f)} = -2.\quad (\text{B13})$$

Besides, for an regular triangle detector,

$$\begin{aligned}\mathcal{R}_a(f) &= \mathcal{R}_b(f), \\ \Gamma_{ab}(f) &= \Gamma_{cd}(f),\end{aligned}\quad (\text{B14})$$

where $a, b, c, d = X, Y, Z$ with $a \neq b \neq c \neq d$.

Based on the above derivation, the transfer function and ORF of AET channel group

$$\begin{aligned}\mathcal{R}_A(f) &= \mathcal{R}_E(f) = \mathcal{R}_X(f) - \Gamma_{XY}(f), \\ \mathcal{R}_T(f) &= \mathcal{R}_X(f) + 2\Gamma_{XY}(f), \\ \Gamma_{AE}(f) &= \Gamma_{AT}(f) = \Gamma_{ET}(f) = 0.\end{aligned}\quad (\text{B15})$$

The last line of Eq. (B15) shows that there is no correlation between the responses of A, E and T to SGWB, and

$$\mathcal{R}_a(f) = -2\Gamma_{ab}(f), \quad f \ll f_*.\quad (\text{B16})$$

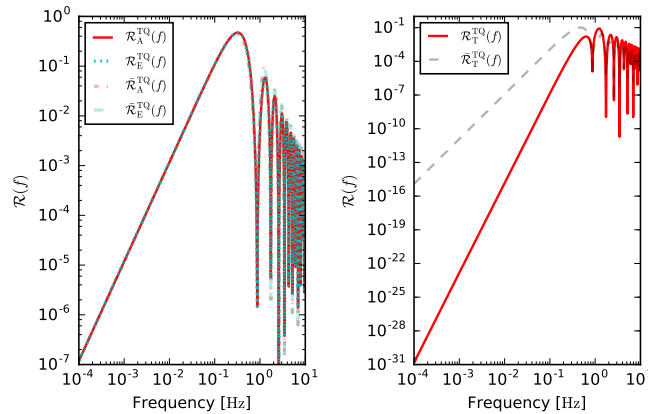


FIG. 9. Transfer function of the channel group AET for TianQin.

Thus, the first two lines of Eq. (B15) reduce to

$$\begin{aligned}\mathcal{R}_A(f) &= \mathcal{R}_E(f) = \frac{3}{2}\mathcal{R}_X(f), \\ \mathcal{R}_T(f) &= o(\mathcal{R}_X(f)), \quad f \ll f_*,\end{aligned}\tag{B17}$$

which implies that T acts as a null channel.

Furthermore, take TianQin as example, the transfer functions of channel group AET based on Eq. (18) are shown in Fig. 9. And in order to illustrate the effect of reference interference site on the transfer function, we show the corresponding result within the dashed line, which employs the false response functions:

$$\begin{aligned}\bar{F}_A^P(f, \hat{k}, t_0) &= \frac{1}{\sqrt{2}} [F_Z^P(f, \hat{k}, t_0) - F_X^P(f, \hat{k}, t_0)], \\ \bar{F}_E^P(f, \hat{k}, t_0) &= \frac{1}{\sqrt{6}} [F_X^P(f, \hat{k}, t_0) - 2F_Y^P(f, \hat{k}, t_0) + F_Z^P(f, \hat{k}, t_0)], \\ \bar{F}_T^P(f, \hat{k}, t_0) &= \frac{1}{\sqrt{3}} [F_X^P(f, \hat{k}, t_0) + F_Y^P(f, \hat{k}, t_0) + F_Z^P(f, \hat{k}, t_0)].\end{aligned}\tag{B18}$$

Under the low-frequency approximation, the misuse of analytical form has little effect on A/E channels, but a significant impact on T channel.

Appendix C: Channel noise level

For the one-way tracking built in the space-borne detector, the output mainly consists of four parts [17, 48]:

$$\begin{aligned}\delta l_{ij}(t) &= \psi_{ij}(t) + C_i(t - L_{ij}) - C_j(t) \\ &\quad + n_{ij}^p(t) + n_{ij}^a(t - L_{ij}) - n_{ji}^a(t),\end{aligned}\tag{C1}$$

where L_{ij} is the armlength between satellite i and j , ψ_{ij} specifies the GW signal. C_i , n_{ij}^p and n_{ij}^a are the noises caused by laser frequency, *aggregate* optical-path and *single* proof-mass acceleration, respectively [49]. Since the laser noise cancels in equal-arm Michelson and TDI channels [16, 17], we will constrain our focus on other noises.

Assuming that the PSD of the same type of noise is equal [50]:

$$\langle \tilde{n}_{ij}^\alpha(f) \tilde{n}_{kl}^{\beta*}(f') \rangle = \frac{1}{2} \delta_{\alpha,\beta} \delta_{ij,kl} \delta(f - f') S_\alpha(f),\tag{C2}$$

then the noise PSD of the equal-arm Michelson

$$\bar{P}_{\text{NM}}(f) = 4S_p(f) + 8 \left(\cos^2 \left[\frac{f}{f_*} \right] + 1 \right) S_a(f),\tag{C3}$$

and for the channel group XYZ [24]

$$\begin{aligned}\bar{P}_{\text{nx,y,z}}(f) &= 4 \sin^2 \left[\frac{f}{f_*} \right] \bar{P}_{\text{nm}}(f) \\ &= 16 \sin^2 \left[\frac{f}{f_*} \right] \left[S_{\text{p}}(f) + 2 \left(\cos^2 \left[\frac{f}{f_*} \right] + 1 \right) S_{\text{a}}(f) \right].\end{aligned}\quad (\text{C4})$$

Furthermore, for channel group AET [24]:

$$\begin{aligned}\bar{P}_{\text{na,e}}(f) &= 8 \sin^2 \left[\frac{f}{f_*} \right] \left[\left(\cos \left[\frac{f}{f_*} \right] + 2 \right) S_{\text{p}}(f) + 2 \left(\cos \left[\frac{2f}{f_*} \right] + 2 \cos \left[\frac{f}{f_*} \right] + 3 \right) S_{\text{a}}(f) \right], \\ \bar{P}_{\text{nt}}(f) &= 32 \sin^2 \left[\frac{f}{f_*} \right] \sin^2 \left[\frac{f}{2f_*} \right] \left(S_{\text{p}}(f) + 4 \sin^2 \left[\frac{f}{2f_*} \right] S_{\text{a}}(f) \right).\end{aligned}\quad (\text{C5})$$

However, the two sides of the above equation (Eq. (C3)-Eq. (C5)) cannot be directly equal. Firstly, to make the component noises dimensionally consistent, the acceleration noise $S_{\text{dl}}^{\text{a}}(f) = S_{\text{a}}(f)/(2\pi f)^4$ [51]. Secondly, to make the GW signals in Eq. (A6) and Eq. (C1) consistent, one should divide the optical-path noise and the acceleration noise by $2L$ [52]. Following this rule, the *strain* noise PSD

$$\begin{aligned}S_{\text{n}}^{\text{p}}(f) &= \frac{S_{\text{p}}(f)}{(2L)^2}, \\ S_{\text{n}}^{\text{a}}(f) &= \frac{S_{\text{dl}}^{\text{a}}(f)}{(2L)^2} = \frac{S_{\text{a}}(f)}{(2L)^2(2\pi f)^4},\end{aligned}\quad (\text{C6})$$

which are in units of Hz^{-1} . Then we employ S_{n}^{p} and S_{n}^{a} instead of S_{p} and S_{a} to correct the strain noise PSD:

$$\begin{aligned}P_{\text{nm}}(f) &= \frac{1}{L^2} \left[S_{\text{p}}(f) + 2 \left(\cos^2 \left[\frac{f}{f_*} \right] + 1 \right) \frac{S_{\text{a}}(f)}{(2\pi f)^4} \right], \\ P_{\text{nx}}(f) &= \frac{4 \sin^2 \left[\frac{f}{f_*} \right]}{L^2} \left[S_{\text{p}}(f) + 2 \left(\cos^2 \left[\frac{f}{f_*} \right] + 1 \right) \frac{S_{\text{a}}(f)}{(2\pi f)^4} \right], \\ P_{\text{na}}(f) &= \frac{2 \sin^2 \left[\frac{f}{f_*} \right]}{L^2} \left[\left(\cos \left[\frac{f}{f_*} \right] + 2 \right) S_{\text{p}}(f) + 2 \left(\cos \left[\frac{2f}{f_*} \right] + 2 \cos \left[\frac{f}{f_*} \right] + 3 \right) \frac{S_{\text{a}}(f)}{(2\pi f)^4} \right], \\ P_{\text{nt}}(f) &= \frac{8 \sin^2 \left[\frac{f}{f_*} \right] \sin^2 \left[\frac{f}{2f_*} \right]}{L^2} \left(S_{\text{p}}(f) + 4 \sin^2 \left[\frac{f}{2f_*} \right] \frac{S_{\text{a}}(f)}{(2\pi f)^4} \right).\end{aligned}$$

By setting $S_{\text{tot}}^{\text{a}}(f) = 4S_{\text{a}}(f)$ under the low-frequency approximation [51, 53], the noise PSD of equal-arm Michelson is further expressed as

$$P_{\text{nm}}(f) = \frac{1}{L^2} \left[S_{\text{p}}(f) + \frac{S_{\text{tot}}^{\text{a}}(f)}{(2\pi f)^4} \right], \quad (\text{C7})$$

where the total noise $S_{\text{tot}}^{\text{a}}(f)$ contains the noise at both ends of the link.

On the other hand, the transfer functions of equal-arm Michelson and X can be converted by Eq. (14):

$$\frac{\mathcal{R}_{\text{X}}(f)}{\mathcal{R}_{\text{M}}(f)} = 2(1 - \cos \left[\frac{2f}{f_*} \right]) = 4 \sin^2 \left[\frac{f}{f_*} \right]. \quad (\text{C8})$$

Combined with Eq. (41), Eq. (B17), Eq. (C7) and Eq. (C8), it can be inferred that the detection sensitivity of equal-arm Michelson, X and A are the same under the low-frequency approximation:

$$S_{\text{nm}}(f) = S_{\text{nx}}(f) = S_{\text{na}}(f), \quad f \ll f_*. \quad (\text{C9})$$

In Fig. 10, we show the sensitivity curves of the above channels for TianQin: $h_{\text{n}}(f) = \sqrt{S_{\text{n}}(f)}$. On one hand, the sensitivity curves of equal-arm and TDI Michelson channels are the same below the characteristic frequency f_* . Although the sensitivity curve of T is much lower than that of other channels at low frequencies, both of them are proportional to f^{-2} . On the other hand, the sensitivity of Michelson channels drops around $3f_*$, beyond which T will be no longer treated as a noise monitor [54].

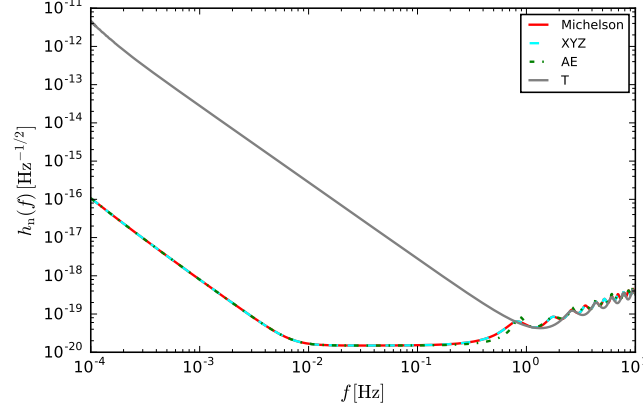


FIG. 10. Sensitivity curve $h_n(f)$ of the channel for TianQin.

Appendix D: Relevant derivation of detection method

For the output from noise-independent channel I and J :

$$\langle \tilde{s}_I(f, t_0) \tilde{s}_J^*(f, t_0) \rangle = \langle \tilde{h}_I(f, t_0) \tilde{h}_J^*(f, t_0) \rangle. \quad (\text{D1})$$

Note that, someone has discussed the subtraction of correlated noise [55, 56]. For simplicity, we prefer to neglect the correlated noise at this stage of the analysis. Then the expectation value and variance $\sigma^2(t)$ of the measurement can be calculated by

$$\begin{aligned} \mu(t_0) &= \langle S_{IJ}(t_0) \rangle \\ &= \int_{t_0-T/2}^{t_0+T/2} dt \int_{-\infty}^{\infty} df \int_{-\infty}^{\infty} df' \langle \tilde{h}_I(f, t_0) \tilde{h}_J^*(f', t_0) \rangle \tilde{Q}_{IJ}(f', t_0) e^{-i2\pi(f-f')t_0} \\ &= \int_{t_0-T/2}^{t_0+T/2} dt \int_0^{\infty} df \int_0^{\infty} df' \delta(f-f') P_{h_{IJ}}(f, t_0) \tilde{Q}_{IJ}(f', t_0) e^{-i2\pi(f-f')t_0} \\ &= T \int_0^{\infty} df P_{h_{IJ}}(f, t_0) \tilde{Q}_{IJ}(f, t_0), \end{aligned} \quad (\text{D2})$$

$$\begin{aligned} \sigma^2(t_0) &= \langle S_{IJ}(t_0) S_{IJ}(\eta_0) \rangle - \langle S_{IJ}(t_0) \rangle \langle S_{IJ}(\eta_0) \rangle \\ &= \int_{t_0-T/2}^{t_0+T/2} dt \int_{\eta_0-T/2}^{\eta_0+T/2} d\eta \int_{-\infty}^{\infty} df \int_{-\infty}^{\infty} df' \int_{-\infty}^{\infty} d\omega \int_{-\infty}^{\infty} d\omega' \\ &\quad \times [\langle \tilde{s}_I(f, t_0) \tilde{s}_I^*(-\omega, \eta_0) \rangle \langle \tilde{s}_J(-f', t_0) \tilde{s}_J^*(\omega', \eta_0) \rangle + \langle \tilde{s}_I(f, t_0) \tilde{s}_J^*(\omega', \eta_0) \rangle \langle \tilde{s}_J(-f', t_0) \tilde{s}_I^*(-\omega, \eta_0) \rangle] \\ &\quad \times \tilde{Q}_{IJ}(f', t_0) \tilde{Q}_{IJ}^*(-\omega', \eta_0) e^{-i2\pi(f-f')t_0} e^{-i2\pi(\omega-\omega')\eta} \\ &= \frac{T}{2} \int_0^{\infty} df \left[(P_{n_I}(f) + P_{h_I}(f, t_0))(P_{n_J}(f) + P_{h_J}(f, t_0)) + |P_{h_{IJ}}(f, t_0)|^2 \right] |\tilde{Q}_{IJ}(f, t_0)|^2 \\ &= \frac{T}{2} \int_0^{\infty} df P_{n_I}(f) P_{n_J}(f) W_{IJ}(f, t_0) |\tilde{Q}_{IJ}(f, t_0)|^2, \end{aligned} \quad (\text{D3})$$

where the correction function is shown in Eq. (29) and the channel noise is assumed to be stationary:

$$\langle \tilde{n}_I(f) \tilde{n}_J^*(f') \rangle = \frac{1}{2} \delta_{IJ} \delta(f-f') P_{n_I}(f) \quad (\text{D4})$$

Combined with Eq. (D2) and Eq. (D3), the square of SNR is obtained by

$$\rho^2(t) = \frac{\mu^2(t)}{\sigma^2(t)} = \frac{2T \left[\int_0^{\infty} df P_{h_{IJ}}(f, t_0) \tilde{Q}_{IJ}(f, t_0) \right]^2}{\int_0^{\infty} df P_{n_I}(f) P_{n_J}(f) W_{IJ}(f, t_0) |\tilde{Q}_{IJ}(f, t_0)|^2}. \quad (\text{D5})$$

By the definition of positive-definite inner product for any pair of complex function $A(f)$ and $B(f)$ [28]:

$$(A, B) := \int_0^\infty df A(f)B^*(f)P_{n_I}(f)P_{n_J}(f)W_{IJ}(f, t_0), \quad (\text{D6})$$

Eq. (D5) turns to

$$\rho^2(t) = 2T \frac{(\tilde{Q}_{IJ}(f, t_0), \frac{P_{h_{IJ}}^*(f, t_0)}{P_{n_I}(f)P_{n_J}(f)W_{IJ}(f, t_0)})^2}{(\tilde{Q}_{IJ}(f, t_0), \tilde{Q}_{IJ}(f, t_0))}. \quad (\text{D7})$$

To maximize the SNR yields the solution:

$$\tilde{Q}_{IJ}(f, t_0) = \lambda \frac{P_{h_{IJ}}^*(f, t_0)}{P_{n_I}(f)P_{n_J}(f)W_{IJ}(f, t_0)} \quad (\text{D8})$$

with a real constant λ and the correction function

$$W_{IJ}(f, t_0) = 1 + \frac{P_{h_I}(f, t_0)P_{n_J}(f) + P_{h_J}(f, t_0)P_{n_I}(f)}{P_{n_I}(f)P_{n_J}(f)} + \frac{P_{h_I}(f, t_0)P_{h_J}(f, t_0) + |P_{h_{IJ}}(f, t_0)|^2}{P_{n_I}(f)P_{n_J}(f)}. \quad (\text{D9})$$

Then the optimal SNR of cross-correlation method is given by Eq. (31). Note that, the correlation time T should be long enough that the PSDs of channel noise $P_n(f)$ and SGWB signal $P_h(f, t_0)$ are nearly invariable in the frequency region $\Delta f \sim 1/T$.

For a single TianQin-like detector, it needs to construct a specific correlator. We start with the auto-correlation of channel group AET

$$\begin{aligned} \langle s_I(f, t_0)s_I(f', t_0) \rangle &= \langle n_I(f)n_I(f') \rangle + \langle h_I(f, t_0)h_I(f', t_0) \rangle \\ &= \frac{1}{2}\delta(f - f')[P_{n_I}(f) + P_{h_I}(f, t_0)], \\ \langle s_T(f)s_T(f') \rangle &= \langle n_T(f)n_T(f') \rangle \\ &= \frac{1}{2}\delta(f - f')P_{n_T}(f), \end{aligned} \quad (\text{D10})$$

where $I = A, E$. At first glance, the auto-correlation PSD P_{h_I} can be obtained by subtracting the second row from the first row of Eq. (D10), which is under the assumption that $P_{n_I}(f) = z_I(f)P_{n_T}(f)$. Just follow that thought line, the reconstructed correlator for null-channel method is written as [57]

$$s_0(t, t') = s_I(t)s_I(t') - \langle n_I(t)n_I(t') \rangle. \quad (\text{D11})$$

The next step is to obtain the measurement:

$$\begin{aligned} K(t_0) &= \sum_{I=A, E} \int_{t_0-T/2}^{t_0+T/2} dt \int_{t_0-T/2}^{t_0+T/2} dt' s_0(t, t')Q_{II}(t - t') \\ &\approx \sum_{I=A, E} \int_{t_0-T/2}^{t_0+T/2} dt \int_{-\infty}^{\infty} df \int_{-\infty}^{\infty} df' [\tilde{s}_I(f, t_0)\tilde{s}_I^*(f', t_0) - \langle \tilde{n}_I(f, t_0)\tilde{n}_I^*(f', t_0) \rangle] \tilde{Q}_{II}(f', t_0)e^{-i2\pi(f-f')t_0} \end{aligned} \quad (\text{D12})$$

of which the expectation value $\mu(t)$ and the variance σ^2 are

$$\begin{aligned}\mu(t_0) &:= \langle K(t_0) \rangle \\ &= \sum_{I=A,E} \int_{t_0-T/2}^{t_0+T/2} dt \int_{-\infty}^{\infty} df \int_{-\infty}^{\infty} df' \langle \tilde{h}_I(f, t_0) \tilde{h}_I^*(f', t_0) \rangle \tilde{Q}_{II}(f', t_0) e^{-i2\pi(f-f')t_0} \\ &= 2T \int_0^{\infty} df P_{h_I}(f, t_0) \tilde{Q}_{II}(f, t_0),\end{aligned}\tag{D13}$$

$$\begin{aligned}\sigma^2(t_0) &= \langle K(t_0)K(\eta_0) \rangle - \langle K(t_0) \rangle \langle K(\eta_0) \rangle \\ &= \sum_{I=A,E} \int_{t_0-T/2}^{t_0+T/2} dt \int_{\eta_0-T/2}^{\eta_0+T/2} d\eta \int_{-\infty}^{\infty} df \int_{-\infty}^{\infty} df' \int_{-\infty}^{\infty} d\omega \int_{-\infty}^{\infty} d\omega' \\ &\quad \times \left[\langle (\tilde{s}_I(f, t_0) \tilde{s}_I^*(f', t_0) - \langle \tilde{n}_I(f, t_0) \tilde{n}_I^*(f', t_0) \rangle) (\tilde{s}_I(\omega, \eta_0) \tilde{s}_I^*(\omega', \eta_0) - \langle \tilde{n}_I(\omega, \eta_0) \tilde{n}_I^*(\omega', \eta_0) \rangle) \rangle \right. \\ &\quad \left. - \langle \tilde{h}_I(f, t_0) \tilde{h}_I^*(f', t_0) \rangle \langle \tilde{h}_I(\omega, \eta_0) \tilde{h}_I^*(\omega', \eta_0) \rangle \right] \tilde{Q}_{II}(f', t_0) \tilde{Q}_{II}^*(\omega', \eta_0) e^{-i2\pi(f-f')t_0} e^{-i2\pi(\omega-\omega')\eta} \\ &= T \int_0^{\infty} df 2(P_{n_I}(f) + P_{h_I}(f, t_0))^2 |\tilde{Q}(f, t_0)|^2 \\ &= 2T \int_0^{\infty} df P_{n_I}^2(f) W_I(f, t_0) |\tilde{Q}_{II}(f, t_0)|^2,\end{aligned}\tag{D14}$$

where the correction function

$$W_I(f, t_0) = \left(1 + \frac{P_{h_I}(f, t_0)}{P_{n_I}(f)} \right)^2.\tag{D15}$$

Compared with Eq. (D9), the correction function $W_I(f, t_0)$ does not involve the cross-term.

When the filter function

$$\tilde{Q}_{II}(f, t_0) = \lambda \frac{P_{h_I}(f, t_0)}{P_{n_I}^2(f) W_I(f, t_0)}\tag{D16}$$

with a real constant λ , the optimal SNR of null-channel method is obtained.

-
- [1] M. Maggiore, *Phys. Rept.* **331**, 283 (2000), arXiv:gr-qc/9909001.
- [2] N. Christensen, *Rept. Prog. Phys.* **82**, 016903 (2019), arXiv:1811.08797 [gr-qc].
- [3] J. D. Romano (2019) arXiv:1909.00269 [gr-qc].
- [4] T. Robson, N. J. Cornish, and C. Liu, *Classical and Quantum Gravity* **36**, 105011 (2019), arXiv:1803.01944 [astro-ph.HE].
- [5] S.-J. Huang, Y.-M. Hu, V. Korol, P.-C. Li, Z.-C. Liang, Y. Lu, H.-T. Wang, S. Yu, and J. Mei, *Phys. Rev. D* **102**, 063021 (2020), arXiv:2005.07889 [astro-ph.HE].
- [6] J. C. N. de Araujo, O. D. Miranda, and O. D. Aguiar, *Phys. Rev. D* **61**, 124015 (2000), arXiv:astro-ph/0004395.
- [7] K. Martinovic, P. M. Meyers, M. Sakellariadou, and N. Christensen, *Phys. Rev. D* **103**, 043023 (2021), arXiv:2011.05697 [gr-qc].
- [8] S. E. Timpano, L. J. Rubbo, and N. J. Cornish, *Phys. Rev. D* **73**, 122001 (2006), arXiv:gr-qc/0504071.
- [9] S. Nissanke, M. Vallisneri, G. Nelemans, and T. A. Prince, *Astrophys. J.* **758**, 131 (2012), arXiv:1201.4613 [astro-ph.GA].
- [10] J. Liu, R.-G. Cai, and Z.-K. Guo, *Phys. Rev. Lett.* **126**, 141303 (2021), arXiv:2010.03225 [astro-ph.CO].
- [11] J. Aasi *et al.* (LIGO Scientific), *Class. Quant. Grav.* **32**, 074001 (2015), arXiv:1411.4547 [gr-qc].
- [12] F. Acernese *et al.* (VIRGO), *Class. Quant. Grav.* **32**, 024001 (2015), arXiv:1408.3978 [gr-qc].
- [13] J. Luo *et al.* (TianQin), *Class. Quant. Grav.* **33**, 035010 (2016), arXiv:1512.02076 [astro-ph.IM].
- [14] P. Amaro-Seoane *et al.* (LISA), (2017), arXiv:1702.00786 [astro-ph.IM].
- [15] M. Tinto and F. B. Estabrook, *Phys. Rev. D* **52**, 1749 (1995).
- [16] M. Tinto and J. W. Armstrong, *Phys. Rev. D* **59**, 102003 (1999).
- [17] J. W. Armstrong, F. B. Estabrook, and M. Tinto, *Astrophys. J.* **527**, 814 (1999).
- [18] R. Hellings and G. Downs, *Astrophys. J. Lett.* **265**, L39 (1983).
- [19] P. F. Michelson, *Monthly Notices of the Royal Astronom-*

- ical Society **227**, 933 (1987).
- [20] N. Christensen, *Phys. Rev.* **D46**, 5250 (1992).
- [21] E. E. Flanagan, *Phys. Rev.* **D48**, 2389 (1993), [arXiv:astro-ph/9305029 \[astro-ph\]](#).
- [22] M. Tinto, J. W. Armstrong, and F. B. Estabrook, *Phys. Rev. D* **63**, 021101 (2001).
- [23] C. J. Hogan and P. L. Bender, *Phys. Rev. D* **64**, 062002 (2001), [arXiv:astro-ph/0104266](#).
- [24] M. Vallisneri and C. R. Galley, *Class. Quant. Grav.* **29**, 124015 (2012), [arXiv:1201.3684 \[gr-qc\]](#).
- [25] N. Seto, *Phys. Rev. D* **102**, 123547 (2020), [arXiv:2010.06877 \[gr-qc\]](#).
- [26] Y. Hu, P.-P. Wang, Y.-J. Tan, and C.-G. Shao, (2022), [arXiv:2209.07049 \[gr-qc\]](#).
- [27] S. L. Larson, W. A. Hiscock, and R. W. Hellings, *Phys. Rev. D* **62**, 062001 (2000), [arXiv:gr-qc/9909080](#).
- [28] B. Allen and J. D. Romano, *Phys. Rev.* **D59**, 102001 (1999), [arXiv:gr-qc/9710117 \[gr-qc\]](#).
- [29] E. Thrane and J. D. Romano, *Phys. Rev. D* **88**, 124032 (2013), [arXiv:1310.5300 \[astro-ph.IM\]](#).
- [30] K. Schmitz, *JHEP* **01**, 097 (2021), [arXiv:2002.04615 \[hep-ph\]](#).
- [31] B. Allen, in *Les Houches School of Physics: Astrophysical Sources of Gravitational Radiation* (1996) pp. 373–417, [arXiv:gr-qc/9604033](#).
- [32] C. W. Misner, K. S. Thorne, and J. A. Wheeler, *Gravitation* (W. H. Freeman, San Francisco, 1973).
- [33] J. D. E. Creighton and W. G. Anderson, *Gravitational-wave physics and astronomy: An introduction to theory, experiment and data analysis* (2011).
- [34] E. Thrane, S. Ballmer, J. D. Romano, S. Mitra, D. Talukder, S. Bose, and V. Mandic, *Phys. Rev. D* **80**, 122002 (2009), [arXiv:0910.0858 \[astro-ph.IM\]](#).
- [35] B. Allen and A. C. Ottewill, *Phys. Rev. D* **56**, 545 (1997), [arXiv:gr-qc/9607068](#).
- [36] N. J. Cornish, *Phys. Rev. D* **65**, 022004 (2002), [arXiv:gr-qc/0106058](#).
- [37] J. D. Romano and N. J. Cornish, *Living Rev. Rel.* **20**, 2 (2017), [arXiv:1608.06889 \[gr-qc\]](#).
- [38] M. Tinto, F. B. Estabrook, and J. W. Armstrong, *Phys. Rev. D* **65**, 082003 (2002).
- [39] M. Tinto and S. V. Dhurandhar, *Living Rev. Rel.* **17**, 6 (2014).
- [40] J. Cheng, E.-K. Li, Y.-M. Hu, Z.-C. Liang, J.-d. Zhang, and J. Mei, *Phys. Rev. D* **106**, 124027 (2022), [arXiv:2208.11615 \[gr-qc\]](#).
- [41] M. R. Adams and N. J. Cornish, *Phys. Rev. D* **82**, 022002 (2010), [arXiv:1002.1291 \[gr-qc\]](#).
- [42] M. R. Adams and N. J. Cornish, *Phys. Rev. D* **89**, 022001 (2014), [arXiv:1307.4116 \[gr-qc\]](#).
- [43] Z.-C. Liang, Y.-M. Hu, Y. Jiang, J. Cheng, J.-d. Zhang, and J. Mei, *Phys. Rev. D* **105**, 022001 (2022), [arXiv:2107.08643 \[astro-ph.CO\]](#).
- [44] E. L. Robinson, J. D. Romano, and A. Vecchio, *Proceedings, 12th Workshop on Gravitational wave data analysis (GWDAW-12): Cambridge, USA, December 13-16, 2007*, *Class. Quant. Grav.* **25**, 184019 (2008), [arXiv:0804.4144 \[gr-qc\]](#).
- [45] C. Cutler, *Phys. Rev. D* **57**, 7089 (1998), [arXiv:gr-qc/9703068](#).
- [46] N. Bartolo *et al.* (LISA Cosmology Working Group), *JCAP* **11**, 009 (2022), [arXiv:2201.08782 \[astro-ph.CO\]](#).
- [47] A. Abramovici *et al.*, *Science* **256**, 325 (1992).
- [48] M. Vallisneri, *Phys. Rev. D* **71**, 022001 (2005), [arXiv:gr-qc/0407102](#).
- [49] A. Krolak, M. Tinto, and M. Vallisneri, *Phys. Rev. D* **70**, 022003 (2004), [Erratum: *Phys.Rev.D* 76, 069901 (2007)], [arXiv:gr-qc/0401108](#).
- [50] S. Chatterji, A. Lazzarini, L. Stein, P. J. Sutton, A. Searle, and M. Tinto, *Phys. Rev. D* **74**, 082005 (2006), [arXiv:gr-qc/0605002](#).
- [51] S. Babak, A. Petiteau, and M. Hewitson, (2021), [arXiv:2108.01167 \[astro-ph.IM\]](#).
- [52] N. J. Cornish and S. L. Larson, *Class. Quant. Grav.* **18**, 3473 (2001), [arXiv:gr-qc/0103075](#).
- [53] X.-C. Hu, X.-H. Li, Y. Wang, W.-F. Feng, M.-Y. Zhou, Y.-M. Hu, S.-C. Hu, J.-W. Mei, and C.-G. Shao, *Class. Quant. Grav.* **35**, 095008 (2018), [arXiv:1803.03368 \[gr-qc\]](#).
- [54] M. Vallisneri, J. Crowder, and M. Tinto, *Class. Quant. Grav.* **25**, 065005 (2008), [arXiv:0710.4369 \[gr-qc\]](#).
- [55] E. Thrane, N. Christensen, R. M. S. Schofield, and A. Effler, *Phys. Rev. D* **90**, 023013 (2014), [arXiv:1406.2367 \[astro-ph.IM\]](#).
- [56] M. W. Coughlin *et al.*, *Class. Quant. Grav.* **33**, 224003 (2016), [arXiv:1606.01011 \[gr-qc\]](#).
- [57] T. L. Smith and R. Caldwell, *Phys. Rev. D* **100**, 104055 (2019), [arXiv:1908.00546 \[astro-ph.CO\]](#).